Friction in Carborane-Based Molecular Rotors Driven by Gas Flow or Electric Field: Classical Molecular Dynamics

Alexandr Prokop,[†,‡] Jaroslav Vacek,[†,‡,*] and Josef Michl[†,‡,*]

[†]Institute of Organic Chemistry and Biochemistry AS CR, v.v.i., Flemingovo nám. 2, 16610 Praha 6, Czech Republic, and [‡]Department of Chemistry and Biochemistry, University of Colorado, Boulder, Colorado 80309-0215, United States

ABSTRACT Friction in molecular rotors is examined by classical molecular dynamics simulations for grid-mounted azimuthal dipolar molecular rotors, whose rotation is either allowed to decay freely or is driven at GHz frequencies by a flow of rare gas or by a rotating electric field. The rotating parts (rotators) are propeller-shaped. Their two to six blades consist of condensed aromatic rings and are attached to a deltahedral carborane hub, whose antipodal carbons carry [*n*]staffane axles mounted on a square molecular grid. The dynamic friction constant η has been derived in several independent ways with similar results. Analysis of free rotation decay yields η as a continuous exponentially decreasing function of rotor frequency. The calculated dependence of friction torque on frequency resembles the classical macroscopic Stribeck curve. Its relation to rotational potential energy barriers and the key role of the rate of intramolecular vibrational redistribution (IVR) of energy and angular momentum from rotator rotation to other modes are considered in two limiting regimes. (i) In the strongly overdamped regime, rotation is much slower than IVR, and effective friction can be expressed through potential barriers to rotation. (ii) In the strongly underdamped regime, rotation is much faster than IVR, whose rate then determines friction.

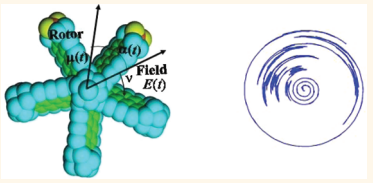

KEYWORDS: molecular rotors · friction · molecular dynamics · potential energy barriers · intramolecular vibrational redistribution

The concept of modular assembly based on molecular construction kits offers an approach to artificial functional materials on the nanoscale. In our version of such a kit,[1−3] analogous to a children's Tinkertoy[4] construction set, molecular grids or scaffolds should result from controlled formation of covalent bonds between straight molecular rods and connectors to which the rods can be attached at fixed regular angles. The scaffolds are to be attached rigidly to a surface and serve as carriers for various active elements, such as turning parts.[3,5−8]

Molecules containing rotating parts are often referred to as "molecular rotors". Those of interest to us presently consist of two covalently connected entities that can rotate relative to each other about a common axle. The part with the smaller moment of inertia about the axle is called the rotator, and the part with the larger moment of inertia is the stator. When the stator is rigidly attached to a macroscopic surface, its moment of inertia is essentially infinite on a molecular scale. Computational simulations suggest that when the rotator carries an electric dipole moment transverse to the axle, it can be driven at GHz frequencies by a rotating electric field,[9,10] and when it is axially chiral (propeller-shaped), it can be driven at similar frequencies by a stream of fluid directed along the axle.[7] Such molecular rotors are much smaller and much less complex than the natural protein motors, which are driven at slow rates by chemical reactions and have received considerable experimental[11] and theoretical[12,13] attention. They are also distinct from the catenane and rotaxane type rotors of Leigh,[14−17] in which the stator and the rotator are not covalently linked, and are conceptually closer to the molecular rotors reported by Kelly,[18,19] Feringa,[20,21] Garcia-Garibay,[22] and to some degree the very simple rotors investigated recently by Sykes.[23,24]

Regular three-dimensional or two-dimensional arrays of dipolar rotors are of even more interest than noninteracting individual rotors, especially if ferroelectric. They could respond to electric fields at a variety of frequencies as light polarization modulators and other optoelectronic components. Surface-mounted altitudinal molecular rotors ("molecular paddle wheels"), driven by oscillating electric field,[25,26] fluid flow,[27,28] or light absorption,[29−31] might pump a thin layer of a fluid. Still other molecular paddle wheels and rotors have been theoretically considered by Král.[32] Modeling of such rotor assemblies[33−40] requires a prior phenomenological characterization of an individual

* Address correspondence to michl@eefus.colorado.edu.

Received for review October 7, 2011 and accepted February 2, 2012.

Published online February 02, 2012
10.1021/nn300003x

rotor, particularly the friction constant, and we attempt to achieve this by means of classical molecular dynamics (MD).

The general concept of friction[41] on a molecular scale has received considerable attention,[42,43] but to our knowledge, friction in molecular rotors has not been examined in detail and the quantitative validity of macroscopic concepts such as a friction coefficient remains unclear. Dynamic friction in a molecular rotor is dictated by the rate at which driving energy and angular momentum need to be supplied to the rotator to compensate for their continual loss to other modes of motion if a steady rotation is to be maintained. For dipolar rotors mounted on an insulator surface, the dominant friction source is nuclear, that is, transfer of energy and momentum from the rotating dipole to other modes of vibrational, librational, and rotational freedom in the molecule,[9,10] whereas for dipolar rotors mounted on a metal surface, it is electronic, that is, transfer from the rotating dipole to the electrons in the metal.[25]

We examine how various structural features affect the performance of rotors based on a carborane[44] hub and how friction operates in molecular rotors and in molecular machines generally.

STRUCTURES AND PROCEDURES

Propeller-Shaped Molecular Rotors. A flow-driven azimuthal rotator should be synthetically accessible, chiral, and not easily racemizable and should have a sizable dipole moment. The blades should be rigid, large, inclined relative to the rotational axis, mechanically approximately balanced, and stiffly attached to the axle, which in turn should be rigidly attached to a molecular grid, preferably at both ends to avoid pendulum-like motion. The mounting grid should not shade the propeller from the incoming gas atoms excessively. The principal unknowns that require optimization are the number and size of blades, their angle of inclination, the size of the dipole, and the mode of attachment to the grid.

We initially examined[7,9] a propeller-shaped octahedral complex of rhenium with two *o*-phenanthrolines as blades. Presently, we report results of MD simulations of rotors based on carboranes **1** (10-vertex 1,10-dicarba-*closo*-decaborane $C_2B_8H_{10}$), **2** (12-vertex 1-carba-*closo*-dodecaborate anion $CB_{11}H_{12}^-$), **3** (14-vertex 1-carba-*closo*-tetradecaborate anion $CB_{13}H_{14}^-$), and **4** (14-vertex 1,14-dicarba-*closo*-tetradecaborane $C_2B_{12}H_{14}$), which permit a symmetrical attachment of two, three, four, five, or six symmetrically disposed charge-carrying blade-shaped divalent substituents **a**–**d**, arranged to provide a large dipole moment and overall electroneutrality. The charges are carried by tetracoordinate N^+ and B^- atoms (Figure 1 and Table 1; see Supporting Information for additional detail). Most work was done with blades **a** and **c**, for which we presently report detailed results.

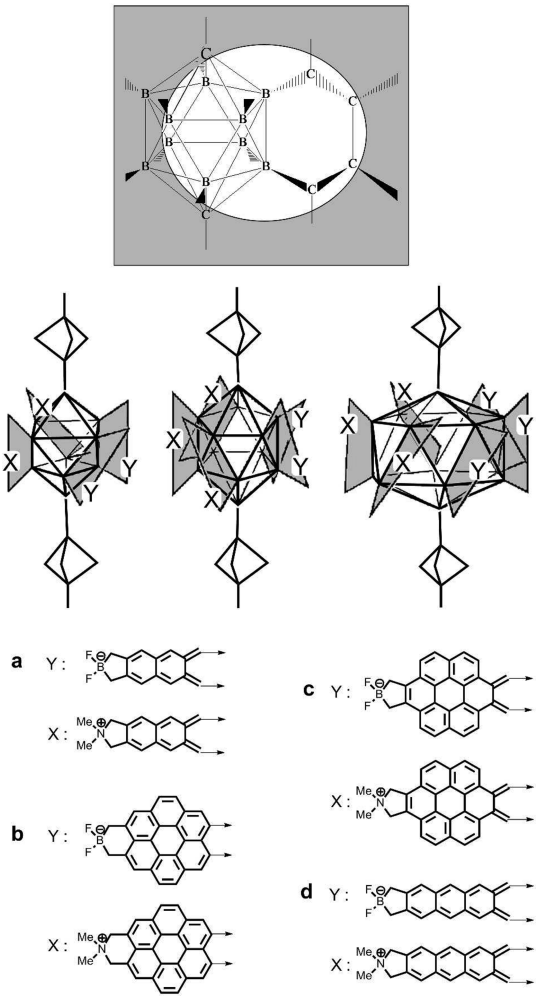

Figure 1. Rotator (propeller) structures. Mode of attachment of blades a–d to a 10-, 12-, or 14-vertex *closo*-carborane hub. Top: detail of the attachment.

TABLE 1. Rotator Structures

rotator[a]	A (Å^2)[b]	ϕ (deg)[c]	I_z (10^3 uÅ^2)[d]	μ (D)[e]
10a4	320	22	56	40
10c4	470	24 (38[f])	127	37
12a5	400	37	77	89
12b5	550	37	130	76
12c5	590	47	153	67
12d5	490	37	89	101
14a6	470	32	94	113

[a] The first number indicates the number of vertices in the *closo* carborane at the hub of the propeller; the letter denotes the blade structure (Figure 1), and the second number gives the total number of blades. [b] Approximate total blade area. [c] Approximate blade inclination angle. [d] The moment of inertia relative to the z axis (u is the atomic mass unit). [e] Approximate dipole moment. [f] Undeformed (nonstacked) blades.

The parent carboranes **1** and **2** and the aromatic structures of the blades are known. Chiral multiply substituted carboranes are not, but the attachment of a single benzene or naphthalene ring has been described,[45,46] and recent synthetic advances[47] suggest that propeller-shaped structures could be made using

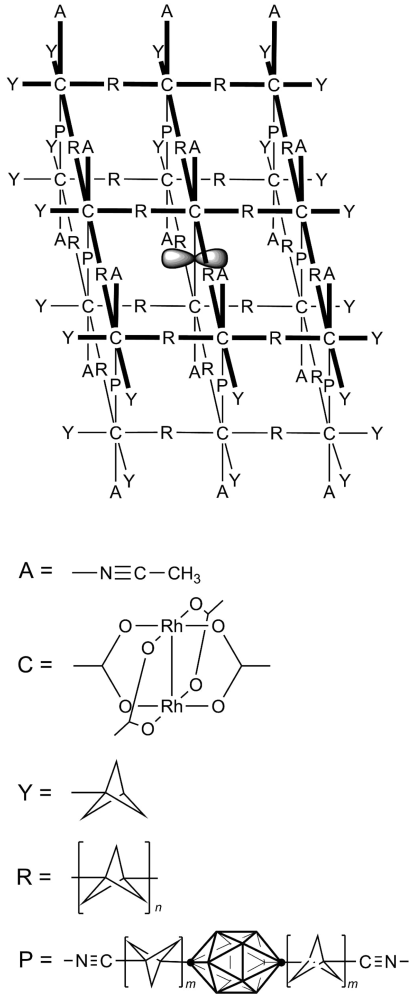

Figure 2. Molecular rotor design with a rotator mounted on a double square grid. See Figure 1 for the details of rotator structure.

known reactions. Structures **3** and **4** also appear realistic because calculations suggested that 14-vertex carboranes will be stable,[48] and the first ones have now been prepared.[49]

The carborane symmetry axis is mounted at both ends to a double grid through three-fold symmetric links with low rotational barriers. The grid is based on the Rh_2^{4+} [*n*]staffanedicarboxylate motif that we used previously.[7,9] Such Rh_2^{4+} connectors[50−52] have seen use in crystalline metallo-organic frameworks,[53,54] and [*n*]staffane rods are also available.[3] Progress toward open molecular grids in many laboratories[55−60] suggests that the grid adopted here (Figure 2) is realistic.

We experimented with three grid sizes (**A**, **B**, **C**; see Supporting Information) and selected the largest one (**C**, 28 Å square side and 27 Å layer separation) for a detailed examination. The propeller-grid assemblies ("molecular rotors") are labeled by symbols such as **C12a5**, where **C** specifies the grid size, **12** states the number of vertices in the carborane in the propeller hub, **a** shows the blade structure (Figure 1), and **5** is the total number of blades in the propeller.

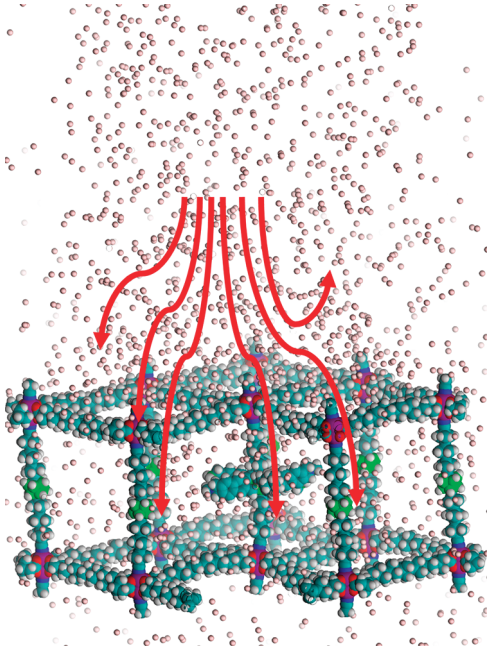

Figure 3. Molecular rotor C12a5 in a stream of He gas (size: 79 Å × 79 Å × 46 Å) with sample gas atom trajectories.

For examples, see Figure 3 and two animations (Supporting Information).

Molecular Dynamics (MD). We used the MD program TINK,[7] based largely on the MOIL 6.2 program of Elber *et al.*,[61] and the universal force field (UFF) potential energy and charge equilibration scheme of Rappé *et al.*[62,63] The definitions of the properties monitored follow our previous work.[7,9,10]

Electric-Field-Driven Rotation. An electric field E (108−11 961 kV cm^{-1}) was taken to rotate in the xy plane, perpendicular to the rotator (propeller) axis z, at a frequency ν (3−150 GHz) and an angular frequency of $\omega = 2\pi\nu$.

The driving torque N acting on the in-plane component of the propeller dipole moment μ is

$$\boldsymbol{N}_p^{\text{field}} = \boldsymbol{E} \times \boldsymbol{\mu} \qquad (1)$$

where boldface symbols indicate vectors.

In the steady state, N_p^{field} is compensated by the friction torque of magnitude $-\eta\omega$ between the stator (the mounting grid) and the rotator. Using α for the angle by which μ lags behind the field,

$$N_p^{\text{field}} = E\mu\sin\alpha = -\eta\omega \qquad (2)$$

The steady state is well behaved in the limit of strong field and/or negligible thermal fluctuations. At fields weaker than the break-off field E_{bo}, the rotator still follows the field but does so irregularly and asynchronously at a frequency lower than that of the rotating electric field.[9,10]

We evaluated η as a function of the field frequency ν from the MD results in a rotating electric field in two different ways. To obtain the approximation $\eta_s(\nu)$, we replaced sin α in eq 2 with its average value $\langle\sin\alpha\rangle$ and

ω with its average value $\langle\omega\rangle$:

$$\eta_s(\nu) = -E\mu\langle\sin\alpha\rangle/\langle\omega\rangle \quad (3)$$

To obtain the approximation $\eta_a(\nu)$,[9] we evaluated the probability a that the propeller will skip a turn, expressed per turn of the field, $a = \alpha_{tot}/2\pi n$. Here, α_{tot} is the cumulative angle $\alpha(t)$ by which the propeller lags behind the driving field after n turns of the field. This approach is useful if the driving force is fighting friction and not random thermal motion, that is, if $E\mu > kT$, where k is Boltzmann's constant and T is temperature.

Turn skipping is described in terms of thermally activated hopping within a potential defined in a system of axes rotating at the angular frequency ω, and the result for a is[9]

$$a = (p - p')/[\omega + (p - p')] \quad (4)$$

where p and p' are the probabilities of forward and backward hopping (see the Supporting Information for additional detail). In the runs used for the evaluation, the rotor was nearly synchronous with the field ($a < 0.23$), and ν therefore stands not only for the frequency of the field but approximately also for the frequency of the rotor.

Gas-Flow-Driven Rotation. The flow conditions are approximately those of a gas stream near a supersonic nozzle fed by a pressurized room-temperature reservoir. From conservation of angular momentum about the z axis

$$L_z(p) + L_z(\mathrm{gr}) = \int {N_p}^{gas}\mathrm{d}t + \int {N_{gr}}^{gas}\mathrm{d}t = -\Sigma_i^m {L_z}^i(g) \quad (5)$$

where ${N_p}^{gas}$ and ${N_{gr}}^{gas}$ denote the torques induced by the flow of gas in the propeller-shaped rotator and the grid, respectively, m is the number of gas particles in the system, and ${L_z}^i(g)$ is the angular momentum of ith gas molecule relative to the z axis. The angular momentum of the rotator, $L_z(p)$, and of the stator (grid), $L_z(gr)$, satisfy the conditions

$$L_z(\mathrm{p}) = \int {N_p}^{gas}\mathrm{d}t - \int {N_p}^{gr}\mathrm{d}t \quad (6)$$

$$L_z(\mathrm{gr}) = \int {N_{gr}}^{gas}\mathrm{d}t + \int {N_p}^{gr}\mathrm{d}t \quad (7)$$

where ${N_p}^{gr}$ is the torque caused by interaction between the stator and the rotator. For a given gas type, temperature, flow velocity, and density, the values of ${N_p}^{gas}$, ${N_p}^{gr}$, and ${N_{gr}}^{gas}$ are characteristic of a particular molecular rotor. In a flow of gas with no external electric field, the average driving torque $\langle N_d(\mathrm{p})\rangle$ can be associated with the average torque exerted by the gas on the rotator, $\langle {N_p}^{gas}\rangle$.

Conservation of angular momentum requires

$$\langle {N_p}^{gas}\rangle = -\langle N^{fr}\rangle - I_z(\mathrm{p})\mathrm{d}\omega/\mathrm{d}t \quad (8)$$

where $\langle N^{fr}\rangle$ is the average torque due to friction and ω is the angular frequency of the rotor. For a propeller that has attained a steady angular velocity ω_{st}, the second term on the right-hand side of eq 8 is zero and

$$\langle {N_p}^{gas}\rangle = -\langle N^{fr}\rangle = -\eta\omega_{st} \quad (9)$$

Substituting the steady propeller angular velocity ω_{st} with angular velocity averaged over periods of steady rotation encountered during the simulation $\langle\omega_z'\rangle$, where the prime indicates a restriction of the averaging time to the periods of regular motion, we obtain

$${\eta_{st}}^{gas} = -\langle {N_p}^{gas}\rangle/\langle\omega_z'\rangle \quad (10)$$

Propeller friction can be assessed at any frequency by assuming $\langle N^{fr}\rangle = \langle {N_p}^{gr}\rangle$. For the friction coefficient, this gives

$$\eta^{gas} = \langle {N_p}^{gr}\rangle/\langle\omega_z'\rangle \quad (11)$$

Due to the complexity of rotor behavior in gas flow, the data on steady rotation had to be individually selected and processed for each simulation. The resulting η^{gas} and ${\eta_{st}}^{gas}$ values were averaged for several frequency ranges using τ (the rotational period computed over the whole simulation time) or τ/τ' (where τ' is the average rotational period computed over the periods of steady rotation only) as the weight, respectively.

Free Decay of Rotation. The rate of decay of rotator angular momentum $\mathrm{d}L_z/\mathrm{d}t$ or angular velocity ω in the absence of an external driving force also provides a measure of propeller friction:

$$-\mathrm{d}L_z/\mathrm{d}t = {N_p}^{fr} = \eta^{dec}\omega \quad (12)$$

Angular velocity should then decay as

$$\omega(t) = \omega_0\exp(-\eta^{dec}t/I_z) \quad (13)$$

where ω_0 stands for the initial angular velocity of the rotator. Since the friction constant is a sensitive function of the instantaneous rotational frequency, we used a direct evaluation from the change in angular momentum instead:

$$\eta^{dec}(\omega) = -(\mathrm{d}L_z/\mathrm{d}t)/\omega \quad (14)$$

RESULTS

Rotational Barrier. The rotational barrier W is not intrinsic to the rotor but arises from interactions between the rotor and the mounting grid. Its height was estimated at 0.01−0.05 kcal/mol for both **C12a5** and **C12c5** by calculating the potential energy profile for a full revolution of the propeller with a geometry optimized at each angle of rotation (Figure S4 in Supporting Information).

When calculated on the bare grid without a propeller, the grid charge distribution possessed the C_4 symmetry of the grid. In that case, the rotational potential barrier curve of a five-bladed propeller may

show up to 4 × 5 = 20 minima. However, due to small energy differences between the rotamers, only 4 minima usually appear. When the charges were calculated for the whole assembly, no symmetry was present and typically just one shallow minimum was observed.

Flow-Driven Rotation. Examples of results are collected in Table S2 in Supporting Information. As a result of collisions with the grid, which represents a significant obstacle to flow, the gas densities and temperatures below the grid were always lower than those above. The average gas density $\langle d_g(r)\rangle$ peaks above the upper part of the grid, where it is 2−6 times higher than in the region near the propeller. The average velocity $\langle v(r)\rangle$ is distributed much more uniformly.

All runs started with a period of irregular rotor motion of length τ_0 (Table S2). Thereafter, in some cases, the motion remains irregular, and in others, the rotor gradually begins to rotate regularly and attains a steady limiting frequency. A measure of the regularity of the rotation is the difference of the average angular velocity $\langle\omega\rangle$ of the propeller computed over the whole duration of the run and angular velocity $\langle\omega'\rangle$ computed over the steady state period of smooth rotation. The irregularity of propeller rotation R is then

$$R = [\langle\langle\omega'\rangle - \omega)^2\rangle]^{1/2} \quad (15)$$

Another measure of rotation irregularity is $T_{rot}(p)$, which provides a measure of the microscopic irregularity of the angular motion. The efficiency e of the conversion of the kinetic energy of the gas flow into the rotational excitation of the propeller is defined as

$$e = E_k^{rot}(p)/E_k^{V}(g) \quad (16)$$

where $E_k^{rot}(p)$ stands for the kinetic energy of propeller rotation

$$E_k^{rot}(p) = (1/2)I_z\overline{\omega}_z^2 \quad (17)$$

and $E_k^{V}(g)$ is the total kinetic energy of gas particles in a tube of a diameter 40 Å and height 20 Å centered at the propeller. Other measures of efficiency are the average angular momentum $\langle L_z(p)\rangle$ and the temperature equivalent of the rotational kinetic energy, $\langle T_{eq}(p)\rangle$ (Table S2). When the rotor fails to turn regularly, $\langle T_{eq}(p)\rangle$ is close to $\langle T_{tot}(p)\rangle$ and $\langle T_{tot}(gr)\rangle$.

The instantaneous propeller response to the flow of gas during simulation was judged from a graph of time dependence of the angular positions of the N^+ and/or B^- ends of the rotor dipole, the corresponding angular momentum $L_z(p)$ in gas flow, and its integrated value (Figure 4).

Performance of Propeller Designs in Helium Gas Flow (Table S2). The propellers (rotators) in **C10a4**, **C12a5**, and **C14a6** with relatively narrow blades behaved similarly. All were driven by He successfully, but with frequent periods of violent vibration. The performance of **C14a6** was the poorest. An attempt to improve performance by increasing the blade length failed, and **C12d5** behaved similarly as **C12a5**. A reduction of the number of blades was detrimental, and **C14a2** and **C14a3** did not rotate at all. The use of larger blades improved the performance, and **C10c4**, **C12b5**, and **C12c5** rotated well under most conditions.

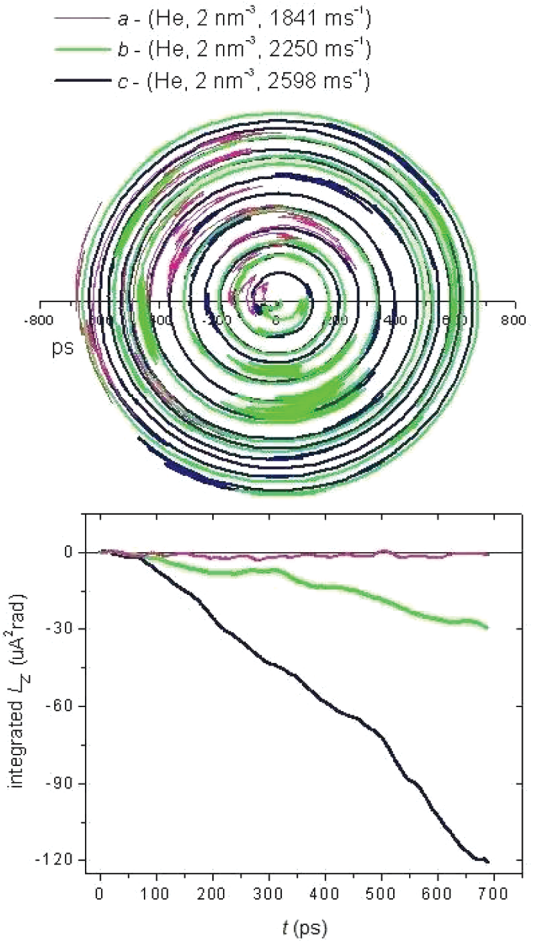

Figure 4. C12c5. Integrated value of the *z* component of propeller angular momentum L_z (bottom) and plot of angular position of a tip of propeller blade against time (top), a: drag dominates over gas driving torque, b: gas driving torque is fighting molecular friction, c: gas driving torque dominates over molecular friction (for details see also Table S2).

In simulations of rotators that were bare and not mounted on a grid, the total angular momentum transferred from gas to the propeller was used as a measure of performance. Table 2 provides a comparison with propellers mounted on grid **C**.

Field-Driven Rotation. Friction coefficients at a series of rotational frequencies are summarized in the Supporting Information, Tables S3 and S4. Since heat is not removed, the temperature of the rotator increases during a simulation run from the initial 300 K and reaches ~350 K at field strengths E below 700 MV m^{-1} and as much as 500 K at E above 700 MV m^{-1}. The gradual heating of a molecular rotor in a rotating

TABLE 2. Performance of Isolated and Grid-Mounted Propellers in a Stream of Gas (He, 2 He/nm^3, 1841m/s)

rotator[a,b]	v_{NC}^T (GHz)[c]	$\int L_z^{NC}dt$ (uÅ^2 rad fs^{-1})[d]	v_C^T (GHz)[e]	$\int L_z^C dt$ (uÅ^2 rad fs^{-1})[f]
10a2	88	47	43.8	37
10a4	75	73	23.7	37
12a5	53	72	23.4	48
14a2	72	39	30.4	27
14a3	69	53	17.7	24
14a6	49	84	13.1	39
C10a4	41	39	22.6	19
C10c4	27	47	12.0	32
C12a5	27	37	9.0	17
C12c5	23	65	16.0	46
C14a6	20	34	2.7	8

[a] The first number indicates the number of vertices of the *closo*-carbaborane that forms the hub of the propeller; the letter denotes the blade structure, and the second number gives the total number of blades. [b] Capital letter in front of a propeller name indicates the mounting grid type. [c] Terminal rotational frequency without charged groups at the tips of propeller blades (F_2B^- and Me_2N^+ replaced with Me_2C). [d] The *z* component of rotator angular momentum integrated over the length of the simulation, without charged groups. [e] Terminal rotational frequency with charged groups at the tips of propeller blades. [f] The *z* component of rotator angular momentum integrated over the length of the simulation, with charged groups.

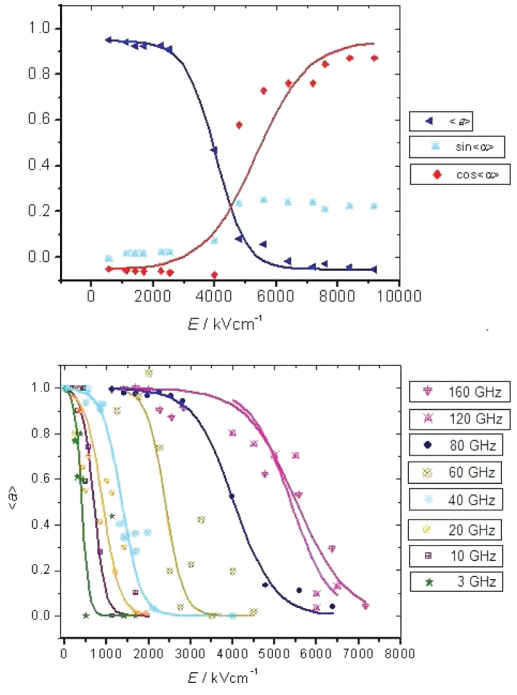

Figure 5. C12a5 rotor performance at various field strengths at 80 GHz (top) and the dependence of average lag per turn $\langle a \rangle$ on field strength for various field frequencies (bottom).

electric field is characterized in Table S5 (Supporting Information).

In the plot of the average lag $\langle a \rangle$ of the rotor behind the field against E (108−11 961 kV cm^{-1}) at a constant field frequency ν (3−160 GHz), $\langle a \rangle$ starts to deviate detectably from unity at the break-off field E_{bo} and reaches 1/*e* at the critical field E_c (Figure 5). These

TABLE 3. Friction Coefficients η for Rotators Mounted on Grid C and Driven by Rotating Electric Field

		ν (GHz)							
rotor	η (eV ps)	3	10	20	40	60	80	120	150
C12a5	η_a	1.44	1.16	1.02	0.94	1.10	1.10	1.12	1.15
	η_s	0.94	0.51	0.34	0.19	0.31	0.26	0.16	0.27
C12c5	η_a	2.08	1.34	1.10	1.44	2.35	2.3	1.74	2.00
	η_s	1.54	0.46	0.44	0.58	0.68	0.61	0.48	0.93

TABLE 4. Friction Coefficients η for Four- and Six-Bladed Rotators Mounted on Grid C and Driven at 10 GHz by Rotating Electric Field

	rotor		
η (eV ps)	C10a4	C10c4	C14a6
η_a	0.71	0.37	1.05
η_s	0.17	0.42	0.33

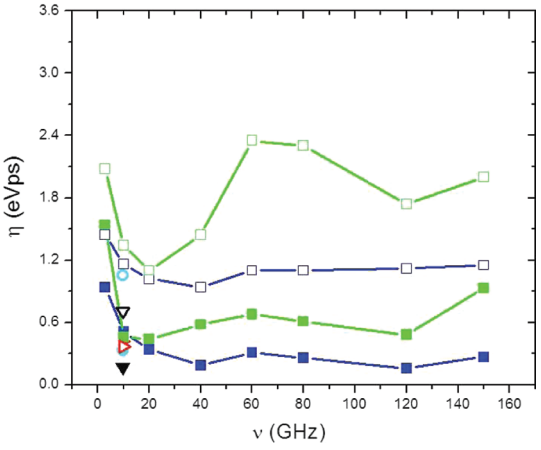

Figure 6. Friction coefficients from simulation in electric field: η_a C12a5 (solid dark blue box); η_a C12c5 (solid green box); η_a C10a4 (solid black triangle); η_a C10c4 (solid red triangle); η_a C14a6 (solid light blue circle); η_s C12a5 (open dark blue box); η_s C12c5 (open green box); η_s C10a4 (open black triangle); η_s C10c4 (open red triangle); η_s C14a6 (open light blue circle).

values are only approximate since $\langle a \rangle$ tends to fluctuate in the transition region between E_{bo} and E_c.

Friction coefficients η_a and η_s were evaluated from $\langle a \rangle$ and $\langle \sin \alpha \rangle$, respectively, obtained from simulations in electric field at ν ranging from 3 to 150 GHz, with field strengths up to 11 MV/cm. Higher frequencies and stronger fields were avoided because preliminary results indicated that the temperature of the system then tends to rise above 450 K. Most calculations were performed for **C12a5** and **C12c5** (Table 3). The rotors **C14a6**, **C10a4**, and **C10c4** were studied in a narrower frequency range as needed for comparison with simulations in gas flow (Table 4).

The calculated values of $\eta_a(\nu)$ and $\eta_s(\nu)$ are shown in Figure 6. The friction coefficient $\eta_a(\nu)$ obtained

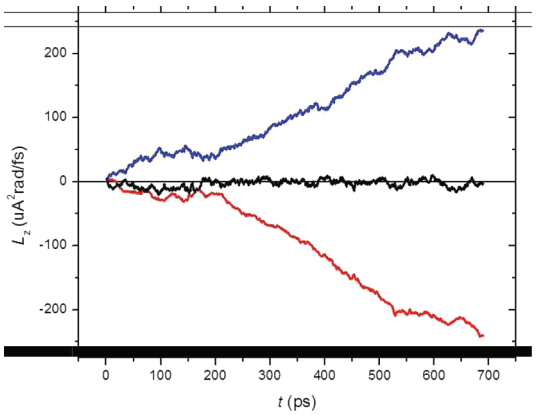

Figure 7. Flow of angular momentum from rotator to grid in C12a5 driven by gas flow (He, 2250 ms^{-1}, 2 He/nm^3). Blue line: integrated N_p^{gas}; red line: integrated N_p^{gr}; black line: L_z of rotator.

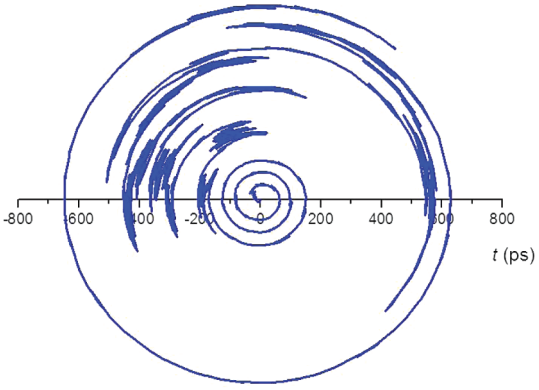

Figure 8. Angular representation of the motion of the nitrogen-carrying tip of C12a5 driven by gas flow (He, 2250 ms^{-1}, 2 He/nm^3).

from a fit of a to the simple model of ref 9, eq 4, is considerably higher than the coefficient $\eta_s(\nu)$ obtained from eq 3. The significance of the $\eta_a(\nu)$ values is limited since they are sensitive to the trial input value of η. The standard deviation of $\eta_a(\omega)$ is as high as ~60% at low to medium frequencies and ~40% at higher frequencies.

Gas-Flow-Driven Rotation. The evaluation of friction in the flow-driven regime spanned a frequency range of about 3–40 GHz, where the highest rotational frequency attainable without overheating the rotor is limited by the gas flow velocity. With He as the driving gas, velocities up to 2600 m/s were necessary. Due to the rotator-grid friction and irregularities in the direction of gas flow as it passes through grid openings, the attainable propeller angular velocities are far below the terminal angular velocity of a solitary propeller. Figure 7 shows the flow of angular momentum between the gas, the rotator, and the grid in the molecular rotor **C12a5**, whose motion is shown in polar representation in Figure 8 (He at 2250 ms^{-1} and gas density of 2 He/nm^3). Integrated N_p^{gas} and N_p^{gr} values and the ratio of their absolute values are shown in Supporting Information (Figure S5).

TABLE 5. Friction Coefficients η for Gas-Flow-Driven Molecular Rotators Mounted on Grid C[a]

		ν (GHz)				
rotor	η (eV ps)	1 – 7	10 ± 3	18 ± 5	28 ± 5	38 ± 5
C10a4	η_{st}^{gas}	0.88	0.29	0.15	0.09	
	η^{gas}	1.03	0.22	0.75	0.37	0.22
C10c4	η_{st}^{gas}		0.27	0.16	0.07	0.07
	η^{gas}	1.19	0.22	0.18	0.09	0.11
C12a5	η_{st}^{gas}		0.20	0.22	0.09	0.04
	η^{gas}		0.22	0.05	0.11	0.04
C12c5	η_{st}^{gas}	0.29	0.31	0.18	0.11	
	η^{gas}	0.11	0.18	0.16	0.11	0.07
C12c5NC	η_{st}^{gas}	0.33	0.18	0.09	0.11	0.07
	η^{gas}	0.31	0.15	0.07	0.04	0.09
C14a6	η_{st}^{gas}	0.59	0.20			
	η^{gas}	0.68	0.40	0.22		
C14a6NC	η_{st}^{gas}	0.33	0.11	0.09		
	η^{gas}	0.31	0.15	0.16		

[a] **NC**: rotors without charged groups at the tips of rotator blades (Me_2N^+ and F_2B^- replaced with Me_2C).

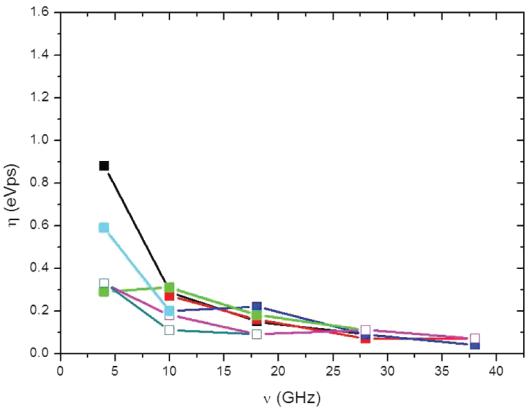

Figure 9. Friction coefficient η_{st}^{gas} from $\langle N_P^{gas} \rangle$ obtained in gas flow as a function of rotational frequency: η_{st}^{gas} C10a4 (black); η_{st}^{gas} C10c4 (red); η_{st}^{gas} C12a5 (dark blue); η_{st}^{gas} C12c5 (green); η_{st}^{gas} C12c5NC (magenta); η_{st}^{gas} C14a6 (light blue); η_{st}^{gas} C14a6NC (yellow).

In a series of runs, for a given gas type, temperature, flow velocity, and density, each rotor was characterized by the values of N_p^{gas}, N_p^{gr}, and N_{gr}^{gas}. Both $\langle N_P^{gas} \rangle$ and $\langle N_P^{gr} \rangle$ were used to evaluate η^{gas} and η_{st}^{gas} in the molecular rotors **C10a4**, **C10c4**, **C12a5**, **C12c5**, and **C14a6**. In order to evaluate the effect of the rotator dipole moment on friction, structures **C12c5NC** and **C14a6NC** in which the charged Me_2N^+ and F_2B^- groups at the tips of the propeller blades were replaced with the electroneutral Me_2C group were also calculated (Table 5). Figures 9 and S6 (Supporting Information) show the friction coefficients derived for rotors driven by gas flow obtained from the steady part and from the total length of the molecular dynamics runs, respectively.

Free Decay of Rotation. Rotation of **C10a4**, **C10c4**, **C12a5**, **C12c5**, and **C14a6** was excited with rotating

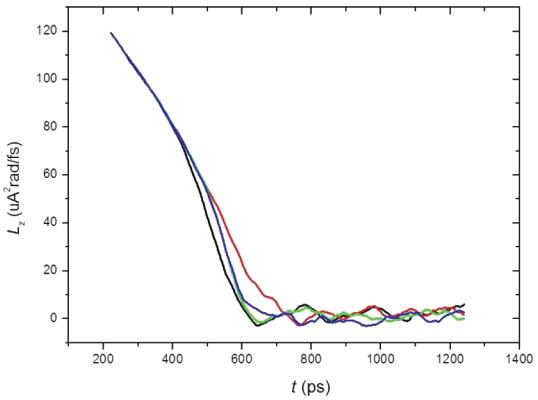

Figure 10. Sample trajectories of free decay of rotation of the rotator in C14a6.

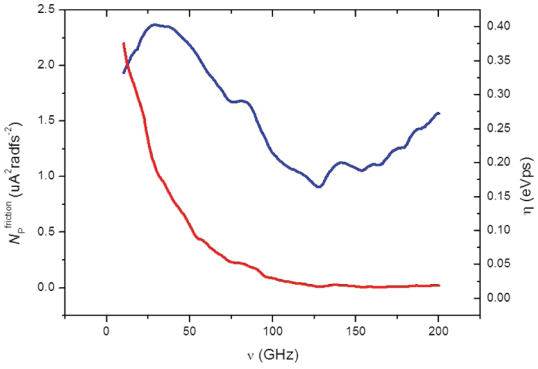

Figure 11. Friction torque $N_p^{friction}$ and friction coefficient η in C12a5 as a function of rotational frequency (red) η^{dec}; (blue) $N_p^{friction}$.

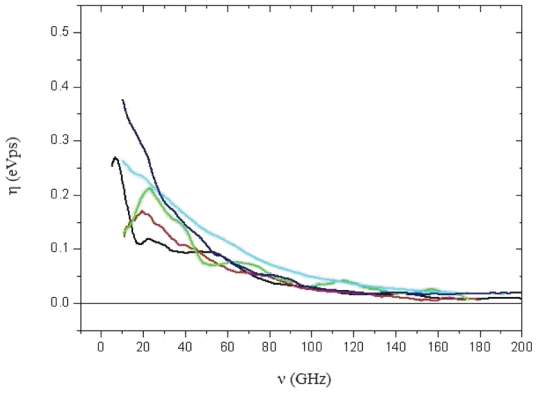

Figure 12. Friction coefficients η from free rotational decay of C10a4 (black); C10c4 (red); C12a5 (dark blue); C12c5 (green); C14a6 (light blue).

electric field, the field was turned off, and $\eta^{dec}(\omega)$ was evaluated from the rate of rotational decay using eq 14. The results for each rotor were smoothed using adjacent averaging with a characteristic span of 1/100 of the total decay time and/or frequency range and subsequently averaged over several decay runs. Figures 10 and S7 show illustrative examples of rotor excitation and subsequent decay trajectories. The course of N_p^{fr} and $\eta^{dec}(\nu)$ for selected rotors is exemplified in Figures 11 and S8 (Supporting Information). The results from rotation decay are summarized in Figure 12 and Table 6.

TABLE 6. Friction Coefficients η^{dec} (eV ps) of Rotators on Grid C from Free Decay

	ν (GHz)						
rotor	10	20	40	60	80	120	150
C12a5	0.38	0.25	0.10	0.05	0.05	0.02	
C12c5	0.14	0.21	0.14	0.10	0.10	0	0
C10a4	0.27	0.11	0.10	0.10	0	0	0
C10c4	0.14	0.16	0.11	0.10	0.10	0	0
C14a6	0.27	0.24	0.18	0.11	0.10	0	0

TABLE 7. Friction in Molecular Rotators Mounted on Grid C at 10 ± 3 GHz

	rotor						
η (eV ps)	C10a4	C10c4	C12a5	C12c5	C12c5NC[a]	C14a6	C14a6NC[a]
η_{ave}^{gas} [b]	0.26	0.25	0.21	0.25	0.16	0.30	0.13
η_a	0.71	0.37	0.51	1.34		1.05	
η_s	0.17	0.42	0.38	0.46		0.33	
η^{dec}	0.27	0.14	0.38	0.14		1.70	

[a] **NC**: rotors without charged groups at the tips of rotator blades (Me_2N^+ and F_2B^- replaced with Me_2C). [b] Value of η_{ave}^{gas} is averaged η_{st}^{gas} and η^{gas}.

TABLE 8. Friction Coefficients η for Rotators Mounted on Grid C Driven by Rotating Electric Field and from Free Rotational Decay

		ν (GHz)							
rotor	η (eV ps)	3	10	20	40	60	80	120	150
C12a5	η_a	1.44	1.16	1.02	0.94	1.10	1.10	1.12	1.15
	η_s	0.94	0.51	0.34	0.19	0.31	0.26	0.16	0.27
	η^{dec}		0.38	0.25	0.10	0.05	0.05	0.02	
C12c5	η_a	2.08	1.34	1.10	1.44	2.35	2.30	1.74	2.00
	η_s	1.54	0.46	0.44	0.58	0.68	0.61	0.48	0.93
	η^{dec}		0.14	0.21	0.14	0.08	0.05	0.03	0.02
C10a4	η_a		0.71						
	η_s		0.17						
	η^{dec}		0.27	0.11	0.10	0.08	0.03	0.02	0.02
C10c4	η_a		0.37						
	η_s		0.42						
	η^{dec}		0.14	0.16	0.11	0.06	0.05	0.02	0.02
C14a6	η_a		1.05						
	η_s		0.33						
	η^{dec}		0.27	0.24	0.18	0.11	0.08	0.03	0.03

Figure S9 in Supporting Information shows a comparison of friction coefficients for **C12a5** estimated under different operating regimes. Results for a series of rotors in the X-band frequency range (10 ± 3 GHz) are summarized in Table 7, which shows averaged values of η^{gas} and η_{st}^{gas} together with η_s, η_a, and η^{dec}. Similar results for five rotors at a series of frequencies are shown in Table 8.

DISCUSSION

Grid Structure. Compared to the previous system,[7] the present rotors offer some advantages, but the maximum angular velocity attainable in a flow of gas is lower, mostly because the second grid layer makes the gas flow at the propeller less regular. Also, the increased overall grid size enhances low-frequency vibrations, and this apparently increases friction. The four-fold grid symmetry shades the blades from the gas flow, especially in **C10a4** and **C10c4**.

Propeller Blade Structure. The total blade shape and area, inclination toward the rotational axis, and number of blades are important. Blades with larger area are more efficient (Tables 2 and S2). Blades **b** and **c** tend to bend at the position of attachment to the carborane, due to strong attractive interactions of adjacent blades with oppositely charged tips. The resulting stacking reduces the dipole moment of the propeller by about 25% compared to **C12a5** and leads to more frequent and stronger fluctuation of the driving torque in rotating electric field, to stronger spatial interaction with the grid, and to a two-fold increase in the rotator moment of inertia. This may be why friction in **C12c5** is higher than in **C12a5** (Table 3) and its η_a varies more. In contrast, the small blades of **C12a5** tend to twist easily, and the torque in gas flow goes quickly to zero as the angle of incidence decreases and can even reverse its sense. The large blades of **C12c5** remain quite effective even at low angles of incidence, and despite their tendency to stack, they tend to twist less frequently and to lesser degree. This may explain why the values of η for **C12a5** and **C12c5** in the gas flow are much closer to each other than in the case of electric-field-driven regime (Table 5).

The inclination angle is more favorable in carboranes with fewer vertices (cf. **10a2** and **14a2** in Table 2). Blade deformation by stacking interaction and Coulombic attraction between the aromatic systems reduce the inclination angles, particularly when there are many blades. These deformations may also enhance rotator shading by the grid, as it can adopt a shape congruent with the grid (Figure S10 in Supporting Information).

When the distance between adjacent blades is close to the mean free path of the gas, some of the gas atoms that impact a blade are seen to scatter onto a neighboring blade, nearly canceling the driving effect of the initial impact. The effects of an increased number of blades and of the overall blade area on performance are therefore not additive (cf. **10a2** and **10a4** in Table 2).

The small difference in friction coefficient η^{dec} between the small **C12a5** and large **C12c5** rotors (Table 6) might be attributed to the higher moment of inertia of the **C12c5** rotator that may partially compensate for stronger propeller−grid interaction in the latter.

Rotor Charges. Some gas flow simulations were repeated with rotators in which the charged F_2B^- and Me_2N^+ groups at blade ends were replaced with neutral Me_2C groups (Figures 9 and S6 and Tables 2, 5, and 7). This charge removal reduced friction significantly and increased the average angular velocity $\langle\omega_z\rangle$ by 10−40% for large blades (**C10c4**, **C12c5**) and by 50−100% for small ones (**C10a4**, **C12a5**). It also improved the effective propeller shape, and **C10a4** and **C12a5** performed nearly twice better than **C10c4** and **C12c5**. In the former two, blade deformation was mostly due to Coulombic interaction and in the latter two to the stacking interaction, largely unaffected by charged group removal.

Driving Fluid. Gas identity, density, and velocity are important. When the energy density of the driving He flow was increased to 125, 150, 175, and 250%, a steadier rotation and up to 3.8 times higher rotational frequencies were achieved for **C12a5**, **C12c5**, and **C14a6**. This trend is more pronounced for **C10c4** and **C12c5** than for **C10a4**, **C12a5**, and **C14a6** because at higher gas velocities the unfavorable stacked conformations of the large blades (**C10c4** and **C12c5**) tend to occur less frequently and there is more resistance to longitudinal vibrations that hamper the effectiveness of the narrow blades (**C10a4**, **C12a5**, **C14a6**). Using increased He gas density to achieve the same gas flow energy density did not produce such improvement (Figure S11 in Supporting Information) because the increased collision rate of gas atoms with the grid led to less regular gas flow at the propeller. This was confirmed by additional improvement in runs with gas density reduced to 75 and 50% and those combining lower He density with increased velocity.

The previously studied system[7] showed that the heavier noble gases rock the propeller and are less capable of driving it into regular motion at the same energy density of gas flow. Our results with Ne show that the carborane propellers handle the stronger collisions with heavier particles much better because of their sturdier attachment to the grid. Since we need higher gas flow energy densities for high propeller efficiency, yet moderate gas densities to keep smooth flow at the propeller, the use of heavier gases deserves further examination.

Friction in Molecular Rotors. We assume the rotators to be nearly rigid objects experiencing thermal motion but acting on the average according to macroscopic equations of motion. Presently, we limit our attention to the driven as opposed to thermal (Brownian) rotational motion regime, in the sense employed in our previous work.[9] In the driven regime, the driving force is strong enough to modify the rotational potential sufficiently to periodically remove any barriers to the rotational motion that may be present in its absence, and such rotors will operate even at 0 K. The origin of dynamic friction experienced by driven molecular rotors is the need to replenish the loss of energy and angular momentum from the rotational mode of motion.

The loss can occur in two ways. (i) Angular momentum could be lost, but energy could remain constant in the rotational mode, associated equally with clockwise and counterclockwise hops and no longer counted as energy of directional rotation, just as the $kT/2$ of such energy present in the rotational mode at equilibrium is not counted. Because of inertia, this contribution to friction is only important if the rotator hardly rotates at all and carries an amount of directed rotational energy comparable to kT. (ii) The energy can flow into other modes of motion and be randomized there. In the molecular rotors investigated here, the rotational energy is moved into intramolecular vibrational modes (nuclear friction). This type of intramolecular energy transfer is often referred to as intramolecular vibrational redistribution (IVR) or, more generally, intramolecular energy redistribution (IER). Recognizing that the IVR time scale in common molecular structures is at most picoseconds or tens of picoseconds, we anticipate that molecular rotors are likely to experience very substantial dynamic friction. When a dipolar rotor is mounted on a metal, most of the energy is moved into electronic degrees of freedom within the conductor (electronic friction),[25] and energy dissipation is even faster.

In addition to dynamic friction, molecular rotors can also experience static friction when they are initially brought from thermal equilibrium into directed rotation. On a molecular scale, static friction results from the potential energy barrier that hinders the internal rotation. In the limit of fast IVR, dynamic and static friction effectively become the same.

The dynamic friction constant η is perhaps the least understood among the properties of molecular rotors and might not even be a valid concept. According to Stokes' law,[64] the friction force on a rotor is a product of η with the angular velocity ω. In a previous simulation of a molecular rotor,[9] we found indications that the friction constant is not actually constant but increases approximately linearly with ω in the region of 3−155 GHz, suggesting an approximately quadratic dependence of the friction force on frequency. The frequency dependence showed additional structure, possibly due to resonances. It is unclear how general this behavior is, and we now examine the validity of the notion of a friction constant in a molecular rotor in more detail.

Comparison of Methods for Friction Constant Evaluation. The alternative analyses of results for rotors driven by an electric field (Figure 6 and Tables 3 and 4), by gas flow (Figures 9 and S6 and Table 5), and freely decaying (Table 6) produced similar results for the dependence of η on ν, and even the numerical values of η mostly lie within an order of magnitude (Tables 7 and 8). Considering how different the methods are, this finding is quite remarkable and suggests that the concept of a friction constant for a molecular rotor is basically sound.

In the region of 3−40 GHz, the values of η^{gas} and $\eta_{st}{}^{gas}$ compare well with η_s. The higher values of η_s might be attributed to lower temperature of the electrically driven rotor, starting mostly at ∼280 K and gradually increasing at a rate that is nearly independent of frequency (Table S5), whereas for the gas-flow-driven rotor, the temperature ranged from 350 to 750 K. Moreover, low-frequency motions are also being excited differently in the two driving modes.

The η_a values show the same general trend but are significantly higher and more scattered than the others, particularly above 40 GHz (Figure S9), perhaps because their evaluation spans a broad range of field strengths, including some where the rotation is very irregular and often completely stops. The values of $\eta^{dec}(\nu)$ compare better with η^{gas} and η_s than with η_a. The elevated values of η^{dec} relative to η^{gas} and $\eta_{st}{}^{gas}$ at low to medium frequencies might again be primarily due to a lower temperature of the rotor (∼200 K) and the absence of a driving torque which can restart the rotor when it stops. At high frequencies, rotor inertia appears to have an opposite effect and lowers the value of η^{dec} considerably below η_s and η_a.

Overall, it seems that the most reliable ways to deduce friction coefficient values for a driven rotor are those that lead to η_s and η^{gas} or $\eta_{st}{}^{gas}$. The magnitude of η^{dec} shows significant deviations to higher values at low frequencies and to lower values at high frequencies.

All values of η represent average behavior, and any one trajectory can deviate considerably, as illustrated in Figure 10. During the initial 200 ps, the several rotation decay trajectories shown for **C14a6** follow the same rate of angular momentum decay, indicating similar values of friction torque, but later they diverge, suggesting sudden random changes in friction in response to an accidental thermally induced change in geometry, which significantly influences the rotor for tens of picoseconds.

Angular Momentum Transfer from Propeller to Grid. In our simulations, the whole rotor structure is allowed to rotate in the xy plane, and the rotator gradually transfers its angular momentum to the grid (Figure 7). If the rotor and the grid happen to lock, as illustrated in Figure 8, the angular momentum of the rotor is transferred to the grid rapidly. Figure S5 gives an example where the transfer in the steady rotational regime is ∼50%, while in the strongly hindered regime or grid lock, it exceeds 95%. Since the rotation is not very stable, the overall value is more than 80%. The lock event becomes more common as the rotor momentum decreases. This may be the cause of the increase of the friction coefficient with decreasing frequency as a general trend.

General Consideration of Friction in Molecular Rotors. In engineering applications, the dependence of the dynamic rotational friction torque on angular velocity (the Stribeck[65,66] curve, Figure 13) is usually modeled as a sum of three friction components: Stribeck friction (a negatively sloped part encountered at low frequencies, right after breakaway or static friction), Coulomb friction (constant), and viscous friction (increasing linearly with velocity).[67,68] Figure 13 provides a

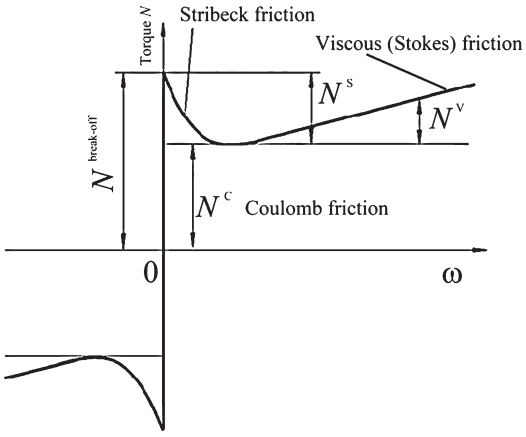

Figure 13. Schematic representation of the Stribeck curve (friction torque as a function of angular frequency).[14]

schematic representation of the three components and also includes static friction.

In physical chemistry, it is usual to define the IVR rate constant k_{IVR} for energy flow from a particular highly excited mode to others as[69]

$$k_{IVR} = \Gamma = 1/(2\pi\tau_{IVR}) \quad (18)$$

where τ_{IVR} is the IVR relaxation time. In statistical IVR, which is likely to occur in large molecular systems, application of the Fermi golden rule leads to

$$k_{IVR}(E) = (2\pi/\hbar)\langle V^2\rangle\rho(E) \quad (19)$$

where ρ is the density of coupled states and $\langle V^2\rangle$ is the magnitude of coupling. In most molecular studies, as E is augmented, the former grows faster than the latter drops, and k_{IVR} is an increasing function of E.

The manner in which friction affects the behavior of an electric-field-driven molecular rotor by removal of energy and angular momentum from the rotational mode depends on the relative size of k_{IVR} and the rotational frequency ν. It is useful to discuss two limits: (i) the strongly overdamped (low frequency) regime, $\nu \ll k_{IVR}$, and (ii) the strongly underdamped (high frequency) regime, $\nu \gg k_{IVR}$. Similar definitions of friction regimes can be obtained for gas flow simulations using flow torque delivered per time unit.

(i) In the **strongly overdamped regime**, the kinetic energy and angular momentum delivered by electric field or gas flow are rapidly removed by IVR, but not fast enough to prevent the rotator from turning when the driving force has removed a barrier. This is realistic in ordinary molecules. Metal-mounted dipolar rotors that were investigated at microwave frequencies[25] belong to this category. In this regime, effective η for a unidirectional driven rotation can be approximated by the sum total of potential energy barriers E_i^B encountered during one complete 360° turn (i = 1,2,...,I). The minimum amount of directional total energy that needs to be added to the thermal energy $(1/2)k_BT$ already present in the rotational mode for a full successful turn is $W = \Sigma_i[E^B - (1/2)k_BT]$, where the sum is over all barriers encountered in a 360° turn. This is ultimately converted to heat and counted as friction. If the field is stronger than this necessary minimum, more energy will be converted to heat and friction will be higher. The minimum work accomplished by the friction torque per cycle is $W = 2\pi N = 2\pi\eta\omega$, where N is the average friction torque, and

$$\eta \geq (1/2\pi\omega)\Sigma_i[E^B - (1/2)k_BT] \quad (20)$$

(ii) In the **strongly underdamped regime**, only a negligible fraction of the kinetic energy delivered by electric field or gas flow is removed by IVR by the time the rotor completes a turn, and η is dictated by k_{IVR}. In principle, it can be calculated from eq 19, with ρ calculated by one of the methods common in applications of RRKM theory.[70] The molecular rotors and frequencies examined in this paper belong to this category.

Determination of k_{IVR} is closely related to our free rotation decay simulation. The difference is that in IVR one follows the loss of energy from an initially excited mode, whereas we deal with unidirectional rotation and measure the loss of angular momentum. The IVR expression is

$$E_{kin}(t) = E_0\exp(-t/\tau_{IVR}) = (1/2)I_z{\omega_0}^2\exp(-t/\tau_{IVR}) \quad (21)$$

while combining $E_{kin} = 1/2I_z\omega^2(t)$ with eq 13 leads to

$$E_{kin}(t) = (1/2)I_z{\omega_0}^2\exp(-2\eta t/I_z) \quad (22)$$

and comparison of the exponents in 21 and 22 yields a relation between the friction coefficient and the rate of IVR

$$\eta(\omega) = I_z/(2\tau_{IVR}) = \pi I_z k_{IVR}(\omega) \quad (23)$$

Figure 10 shows that the free rotation decay is strongly nonexponential and accelerates as the rotor slows down. Without the driving torque, the rotor molecule initially rotating at 200 GHz slows down to thermal motion within less than 450 ps. We find that η decreases roughly exponentially with increasing frequency (Figure 12)

$$\eta = A\exp(-\omega/\omega_0) \quad (24)$$

An example of the interplay between inertia and friction in a rotor driven by rotating electric field is provided in Figure S7. Here, a very strong rotating field was used to start the rotor. Due to its inertia, the rotor took about 3 turns of the field before the it caught up with the field, and then it continued to librate significantly about the field direction. Due to friction, the librational motion gradually decreased. Once the driving electric field was turned off, angular momentum was lost rapidly.

The dependence of the friction torque and friction constant on the frequency of rotation observed for the molecular rotors resembles strongly the macroscopic Stribeck behavior (compare Figures 13 and 11, 12 and S8), in that friction drops with increasing ν. Figure 11 even shows a hint of a transition to Coulomb and Stokes

behavior. This similarity to macroscopic behavior is not a trivial result that follows automatically from the use of classical mechanics to describe a mechanical object because the microscopic nature of the object is taken into account properly (kT is not negligible). We doubt that a result of a quantum calculation would be qualitatively different. The moment of inertia of our rotors is so large that the quantization of rotational motion will have an insignificant effect and the main effict of a quantum mechanical treatment would probably be on the description of the high-frequency CH stretching vibrations. At the molecular level, the initial decrease of the friction coefficient followed by an anticipated increase at higher frequencies most likely results from an interplay of the $\langle V^2 \rangle$ and ρ factors in eq 19, with the former dropping and the latter growing at increasing frequencies. It would be interesting to determine the structural factors that determine which type of friction will dominate the behavior of a molecular rotor, but presently, they are not understood.

SUMMARY

MD simulations show that carborane-based molecular propellers can be successfully driven at GHz rates by rotating electric field or by a flow of a gas, in which structures with two or three blades generally seem to perform better than those with a larger number. Friction constants of carborane-based molecular rotors were estimated using several simple models fitted to molecular dynamics simulation data for electric-field-driven, gas-flow-driven, and freely decaying rotation, with generally similar results. We found that the concept of a friction coefficient for a molecular rotor is approximately valid.

In the range of rotational frequencies investigated, the dependence of friction coefficient on the rotational frequency resembles macroscopic nonlinear low-velocity Stribeck friction, which is reduced as the rotational frequency increases. It is presently not clear under which conditions friction in molecular rotors will resemble Stribeck friction and when it will behave more like Coulomb or Stokes friction.

Intramolecular vibrational energy distribution (IVR) is the cause of friction in molecular rotors, and we have identified two limiting regimes. In the overdamped regime, friction can be expressed in terms of rotational barriers, and in the underdamped regime, it is determined by the rate of IVR.

METHODS

MD calculations were performed with the program TINK[7] using the UFF potential, modified for use with carboranes as explained in the Supporting Information, and the charge equilibration method.[62,63] The VMD program was used for result visualization.[71] The details of the computational procedure used are given in the Supporting Information.

Conflict of Interest: The authors declare no competing financial interest.

Acknowledgment. This project was supported by the DOE (DE-FG02-08ER15959), DoD High Performance Computation Office and USARO projects ARON C1R and ARON C014, the Czech Science Foundation Grant 203/09/1802, Czech Ministry of Education, Youth and Sport Project ME 09020, and the European Research Council (FP7/2007-2013/ERC Grant 227756). We are grateful to Dr. Paul Dron for assistance with the drawing of figures.

Supporting Information Available: Description of the TINK program and UFF modified for carboranes, details of rotor structures, molecular dynamics procedures, and definitions of properties monitored. Tables S1−S5, Figures S1−S11, and animation of **C12c5** alone and in a stream of gas. This material is available free of charge *via* the Internet at http://pubs.acs.org.

REFERENCES AND NOTES

1. Kaszynski, P.; Michl, J. [*n*]Staffanes: A Molecular-Size 'Tinkertoy' Construction Set for Nanotechnology. Preparation of End-Functionalized Telomers and a Polymer of [1.1.1]Propellane. *J. Am. Chem. Soc.* **1988**, *110*, 5225–5226.
2. Michl, J.; Kaszynski, P.; Friedli, A. C.; Murthy, G. S.; Yang, H. C.; Robinson, R. E.; McMurdie, N. D.; Kim, T. Harnessing Strain: From [1.1.1]Propellanes to Tinkertoys. In *Strain and Its Implications in Organic Chemistry*; de Meijere, A., Blechert, S., Eds.; NATO ASI Series; Kluwer: Dordrecht, The Nederlands, 1989; Vol. 273, pp 463−482.
3. Kaszynski, P.; Friedli, A. C.; Michl, J. Towards a Molecular-Size 'Tinkertoy' Construction Set. Methyl [*n*]Staffane-3-carboxylates, Dimethyl [*n*]Staffane-3,3$^{(n-1)}$-dicarboxylates, and [*n*]Staffane-3,3$^{(n-1)}$-dithiols from [1.1.1]Propellane. *J. Am. Chem. Soc.* **1992**, *114*, 601–620.
4. Tinkertoy is a trademark of Playskool, Inc., Pawtucket, RI 02862 USA, and designates a children's toy construction set consisting of straight wooden sticks and other simple elements insertable into a spool-like connectors.
5. Michl, J., Ed. *Modular Chemistry*; Kluwer Academic Publishers: Dordrecht, The Netherlands, 1997; p 1.
6. Zheng, X.; Mulcahy, M. E.; Horinek, D.; Galeotti, F.; Magnera, T. F.; Michl, J. Dipolar and Non-polar Altitudinal Molecular Rotors Mounted on a Au(111) Surface. *J. Am. Chem. Soc.* **2004**, *126*, 4540–4542.
7. Vacek, J.; Michl, J. A Molecular 'Tinkertoy' Construction Kit: Computer Simulation of Molecular Propellers. *New J. Chem.* **1997**, *21*, 1259–1267.
8. Kottas, G. S.; Clarke, L. I.; Horinek, D.; Michl, J. Artificial Molecular Rotors. *Chem. Rev.* **2005**, *105*, 1281–1376.
9. Vacek, J.; Michl, J. Molecular Dynamics Simulation of a Grid-Mounted Molecular Dipolar Rotor in a Rotating Electric Field. *Proc. Natl. Acad. Sci. U.S.A.* **2001**, *98*, 5481–5486.
10. Horinek, D.; Michl, J. Molecular Dynamics Simulation of an Electric Field Driven Dipolar Molecular Rotor Attached to a Quartz Glass Surface. *J. Am. Chem. Soc.* **2003**, *125*, 11900–11910.
11. Noji, H.; Yasuda, R.; Yoshida, M.; Kinosita, K. Direct Observation of the Rotation of F_1-ATPase. *Nature* **1997**, *386*, 299–302.
12. Astumian, R. D. Adiabatic Theory for Fluctuation-Induced Transport on a Periodic Potential. *J. Phys. Chem.* **1996**, *100*, 19075–19081.
13. Makhnovskii, Y. A.; Rozenbaum, V. M.; Yang, D.-Y.; Lin, S. H.; Tsong, T. Y. Flashing Ratchet Model with High Efficiency. *Phys. Rev. E* **2004**, *69*, 02110-1–02110-7.
14. Leigh, D. A.; Wong, J. K. Y.; Dehez, F.; Zerbetto, F. Unidirectional Rotation in a Mechanically Interlocked Molecular Rotor. *Nature* **2003**, *424*, 174–179.

15. Kay, E. R.; Leigh, D. A. Photochemistry: Lighting up Nanomachines. *Nature* **2006**, *440*, 286–287.
16. Kay, E. R.; Leigh, D. A.; Zerbetto, F. Synthetic Molecular Motors and Mechanical Machines. *Angew. Chem., Int. Ed.* **2007**, *46*, 72–191.
17. Lee, C.-F.; Leigh, D. A.; Pritchard, R. G.; Schultz, D.; Teat, S. J.; Timco, G. A.; Winpenny, R. E. P. Hybrid Organic−Inorganic Rotaxanes and Molecular Shuttles. *Nature* **2009**, *458*, 314–318.
18. Kelly, T. R. Progress toward a Rationally Designed Molecular Motor. *Acc. Chem. Res.* **2001**, *34*, 514–522.
19. Kelly, T. R., Ed. *Topics in Current Chemistry*; Springer Verlag: Heidelberg, 2005; Vol. 262.
20. Feringa, B. L. In Control of Motion: From Molecular Switches to Molecular Motors. *Acc. Chem. Res.* **2001**, *34*, 504–513.
21. Browne, W. R.; Feringa, B. L. Light Switching of Molecules on Surfaces. *Annu. Rev. Phys. Chem.* **2009**, *60*, 407–428.
22. Khuong, T.-A. V.; Nuñez, J. E.; Godinez, C. E.; Garcia-Garibay, M. A. Crystalline Molecular Machines: A Quest toward Solid-State Dynamics and Function. *Acc. Chem. Res.* **2006**, *39*, 413–422.
23. Tierney, H. L.; Calderon, C. E.; Baber, A. E.; Sykes, E. C. H.; Wang, F. Understanding the Rotational Mechanism of a Single Molecule: STM and DFT Investigations of Dimethyl Sulfide Molecular Rotors on Au(111). *J. Phys. Chem. C* **2010**, *114*, 3152–3155.
24. Tierney, H. L.; Murphy, C. J.; Jewell, A. D.; Baber, A. E.; Iski, E. V.; Khodaverdian, H. Y.; McGuire, A. F.; Klebanov, N.; Sykes, E. C. H. Experimental Demonstration of a Single-Molecule Electric Motor. *Nat. Nanotechnol.* **2011**, *6*, 625–629.
25. Horinek, D.; Michl, J. Surface Mounted Altitudinal Molecular Rotors in Alternating Electric Field: Single-Molecule Parametric Oscillator Molecular Dynamics. *Proc. Natl. Acad. Sci. U.S.A.* **2005**, *102*, 14175–14180.
26. Vacek, J.; D. Horinek, D.; Michl, J. Molecular Dynamics of a Fast Artificial Electric-Field Driven Surface-Mounted Molecular Rotor: A Single-Molecule Parametric Oscillator. In *Foundations of Nanoscience: Self-Assembled Architectures and Devices*; Reif, J., Ed.; ScienceTechnica: Durham, NC, 2005; pp 241−245.
27. Vacek, J.; Horinek, D.; Michl, J. Calculations of Molecular Rotors and Motors. *Proceedings of the HPCMP Users Group Conference*; IEEE Computer Society: Los Alamitos, CA, 2005; pp 1−8.
28. Vacek, J.; Chocholoušová, J.; Michl, J. Calculations for a Gas-Flow Driven Molecular Rotor. *Proceedings of the HPCMP Users Group Conference*; IEEE Computer Society: Los Alamitos, CA, 2007; pp 153−157.
29. Vacek, J.; Kobr, L.; Miller, J.; Michl, J. Design of a Fast Artificial Light-Absorption Driven Molecular Rotor. In *Foundations of Nanoscience: Self-Assembled Architectures and Devices*; Reif, J., Ed.; ScienceTechnica: Durham, NC, 2005; pp 233−237.
30. Vacek, J.; Chocholoušová, J.; Kobr, L.; Miller, J.; Michl, J. Calculations of Light-Absorption Driven Molecular Rotors. *Proceedings of the HPCMP Users Group Conference*; IEEE Computer Society: Los Alamitos, CA, 2006; pp 193−196.
31. Vacek, J.; Michl, J. Artificial Surface-Mounted Molecular Rotors: Molecular Dynamics Simulations. *Adv. Funct. Mater.* **2007**, *17*, 730–739.
32. Wang, B. Y.; Král, P. Chemically Tunable Nanoscale Propellers of Liquids. *Phys. Rev. Lett.* **2007**, *98*, 266102-1–266102-4.
33. Rozenbaum, V. M.; Ogenko, V. M.; Chuiko, A. A. Vibrational and Orientational States of Surface Atomic Groups. *Sov. Phys. Usp.* **1991**, *34*, 883–902.
34. Zorski, H.; Infeld, E. *Phys. Rev. Lett.* **1997**, *68*, 1180–1183.
35. DeLeeuw, S. W.; Solvaeson, D.; Ratner, M. A.; Michl, J. Molecular Dipole Chains: Excitations and Dissipation. *J. Phys. Chem. B* **1998**, *102*, 3876–3885.
36. Sim, E.; Ratner, M. A.; de Leeuw, S. W. Molecular Dipole Chains II. *J. Phys. Chem. B* **1999**, *103*, 8663–8670.
37. *Molecular Electronics: Science and Technology*; Aviram, A., Ratner, M. A., Eds.; New York Academy of Sciences: New York, 1998.
38. *Molecular Electronics II*; Aviram, A., Ratner, M. A., Mujica, V., Eds.; New York Academy of Sciences: New York, 2002.
39. de Jonge, J. J.; Ratner, M. A.; de Leeuw, S. W.; Simonis, R. O. Molecular Dipole Chains III: Energy Transfer. *J. Phys. Chem. B* **2004**, *108*, 2666–2675.
40. de Jonge, J. J.; Ratner, M. A.; de Leeuw, S. W. Local Field Controlled Switching in a One-Dimensional Dipolar Array. *J. Phys. Chem. C* **2007**, *111*, 3770–3777.
41. Halling, J., Ed. *Principles of Tribology*; MacMillan Press: London, 1978.
42. Carpick, R. W.; Salmeron, M. Scratching the Surface: Fundamental Investigations of Tribology with Atomic Force Microscopy. *Chem. Rev.* **1997**, *97*, 1163–1194.
43. Devaprakasam, D.; Hatton, P. V.; Möbus, G.; Inkson, B. J. Nanoscale Tribology, Energy Dissipation and Failure Mechanisms of Nano- and Micro-silica Particle-Filled Polymer Composites. *Tribol. Lett.* **2009**, *34*, 11–19 and references therein.
44. Grimes, R. N. *Carboranes*, 2nd ed.; Elsevier: Amsterdam, 2011.
45. Wu, S.; Jones, M., Jr. A Carbon-to-Boron-Bridged Benzo-*o*-Carborane. *Inorg. Chem.* **1988**, *27*, 2005–2008.
46. Donald, S.; Matteson, S. D.; Davis, R. A. Synthesis and Properties of 1,2-(2,3-Naphtho)-*o*-Carborane. *Inorg. Chem.* **1974**, *13*, 859–862.
47. King, B. T.; Körbe, S.; Schreiber, P. J.; Clayton, J.; Nemcová, A.; Havlas, Z.; Vyakaranam, K.; Fete, M. G.; Zharov, I.; Ceremuga, J.; Michl, J. The Sixteen $CB_{11}H_nMe_{12-n}^-$ Anions with Five-Fold Substitution Symmetry: Anodic Oxidation and Electronic Structure. *J. Am. Chem. Soc.* **2007**, *129*, 12960–12980.
48. Schleyer, P. R.; Najafian, K.; Mebel, A. M. The Large *closo*-Borane Dianions, $B_nH_n^{2-}$ (n = 13−17) Are Aromatic, Why Are They Unknown? *Inorg Chem.* **1998**, *37*, 6765–6772.
49. Deng, L.; Chan, H. S.; Xie, Z. Synthesis, Reactivity, and Structural Characterization of a 14-Vertex Carborane. *Angew. Chem., Int. Ed.* **2005**, *44*, 2128–2131.
50. Dunbar, K. R. Spectroscopic and Structural Investigation of the Unbridged Dirhodium Cation $[Rh_2(CH_3CN)_{10}]^{4}$. *J. Am. Chem. Soc.* **1988**, *110*, 8247–8249.
51. Cotton, F. A.; Walton, R. A. *Multiple Bonds between Metal Atoms*; Clarendon Press: Oxford, 1993; Chapter 7.
52. Magnera, T. F.; Pecka, J.; Michl, J. In *Science and Technology of Polymers and Advanced Materials*; Prasad, P. N., Mark, J. E., Kandil, S. H., Kafafi, Z. H., Eds.; Plenum Press: New York, 1998; p 385.
53. Mori, W.; Hoshino, H.; Nishimoto, Y.; Takamizawa, S. Synthesis and Gas Occlusion of New Micropore Substance Rhodium(II) Carboxylates Bridged by Pyrazine. *Chem. Lett.* **1999**, *28*, 331–332.
54. Takamizawa, S.; Hiroki, T.; Nakata, E.; Mochizuki, K.; Mori, W. Crystal Structure and Gas Adsorption Property of Rhodium(II) Benzoate Pyrazine. *Chem. Lett.* **2002**, *31*, 1208–1209.
55. De Feyter, S.; De Schryver, F. C. Two-Dimensional Supramolecular Self-Assembly Probed by Scanning Tunneling Microscopy. *Chem. Soc. Rev.* **2003**, *32*, 139–150.
56. Bonifazi, D.; Enger, O.; Diederich, F. Supramolecular [60]Fullerene Chemistry on Surfaces. *Chem. Soc. Rev.* **2007**, *36*, 390–414.
57. Li, S.-S.; Northrop, B. H.; Yuan, Q.-H.; Wan, L.-J.; Stang, P. J. Surface Confined Metallosupramolecular Architectures: Formation and Scanning Tunneling Microscopy Characterization. *Acc. Chem. Res.* **2009**, *42*, 249–259.
58. Klyatskaya, S.; Klappenberger, F.; Schlickum, U.; Kühne, D.; Marschall, M.; Reichert, J.; Decker, R.; Krenner, W.; Zoppellaro, G.; Brune, H.; Barth, J. V.; Ruben, M. Surface-Confined Self-Assembly of Di-carbonitrile Polyphenyls. *Adv. Funct. Mater.* **2011**, *21*, 1230–1240.
59. Michl, J.; Magnera, T. F. Two-Dimensional Supramolecular Chemistry with Molecular Tinkertoys. *Proc. Natl. Acad. Sci. U.S.A.* **2002**, *99*, 4788–4792.

60. Varaksa, N.; Pospisil, L.; Magnera, T. F.; J. Michl, J. Self-Assembly of a Metal Ion Bound Monolayer of Trigonal Connectors on Mercury. An Electrochemical Langmuir Trough. *Proc. Natl. Acad. Sci. U.S.A.* **2005**, *99*, 5012–5017.
61. Elber, R.; Roitberg, A.; Simmerling, C.; Goldstein, R.; Li, H.; Verkhivker, G.; Keasar, C.; Zhang, J.; Ulitsky, A. *MOIL 6.2*; Hebrew University, Jerusalem, Israel, 1994.
62. Rappé, A. K.; Casewit, C. J.; Coldwell, K. S.; Goddard, W. A., III; Skiff, W. M. UFF, a Full Periodic Table Force Field for Molecular Mechanics and Molecular Dynamics Simulations. *J. Am. Chem. Soc.* **1992**, *114*, 10024–10035.
63. Rappé, A. K.; Goddard, W. A., III. Charge Equilibration for Molecular Dynamics Simulations. *J. Phys. Chem.* **1991**, *95*, 3358–3363.
64. Dowson, D. *History of Tribology*, 2nd ed.; American Society of Mechanical Engineers: New York, 1999.
65. Stribeck, R. Ball Bearings for Any Stress. *Z. des VDI* **1901**, *45*.
66. Stribeck, R. Characteristics of Plain and Roller Bearings. *Z. des VDI* **1902**, *46*.
67. Armstrong, B.; de Wit, C. C. In *The Control Handbook*; Levine, W. S., Ed.; CRC Press: Boca Raton, FL, 1996; p 1369.
68. http://www.mathworks.com.
69. Bixon, M.; Jortner, J. Intramolecular Radiationless Transitions. *J. Chem. Phys.* **1968**, *48*, 715–726.
70. Wadi, H.; Pollak, E. Accurate Computation of Quantum Densities of States and RRKM Rate Constants for Large Polyatomic Molecules: The STAIR Method. *J. Chem. Phys.* **1999**, *110*, 8246–8253.
71. Humphrey, W.; Dalke, A.; Schulten, K. VMD - Visual Molecular Dynamics. *J. Mol. Graphics* **1996**, *14*, 33–38. http://www.ks.uiuc.edu/Research/vmd/.